Available online at www.sciencedirect.com
ScienceDirect
Journal of Computational Physics 227 (2008) 7089–7112
JOURNAL OF COMPUTATIONAL PHYSICS
www.elsevier.com/locate/jcp

Nonstationary phase boundary estimation in electrical impedance tomography using unscented Kalman filter

Umer Zeeshan Ijaz [a], Anil Kumar Khambampati [a], Jeong Seong Lee [b], Sin Kim [b], Kyung Youn Kim [a,*]

[a] Department of Electronic Engineering, Cheju National University, Cheju 690-756, Republic of Korea
[b] Department of Nuclear and Energy Engineering, Cheju National University, Cheju 690-756, Republic of Korea

Received 31 August 2007; received in revised form 27 December 2007; accepted 30 December 2007
Available online 12 January 2008

Abstract

In this paper, an effective nonstationary phase boundary estimation scheme in electrical impedance tomography is presented based on the unscented Kalman filter. The inverse problem is treated as a stochastic nonlinear state estimation problem with the nonstationary phase boundary (state) being estimated online with the aid of unscented Kalman filter. This research targets the industrial applications, such as imaging of stirrer vessel for detection of air distribution or detecting large air bubbles in pipelines. Within the domains, there exist "voids" having zero conductivity. The design variables for phase boundary estimation are truncated Fourier coefficients. Computer simulations and experimental results are provided to evaluate the performance of unscented Kalman filter in comparison with extended Kalman filter to show a better performance of the unscented Kalman filter approach.

AMS classification: 65K99; 93E11; 93E24

Keywords: Electrical impedance tomography; Boundary estimation; Extended Kalman filter; Unscented Kalman filter

1. Introduction

Flow of a mixture of two fluids in pipes is of great interest to researchers. The liquid–gas or liquid-vapor mixtures are encountered in condensers and evaporators, gas–liquid reactors, and combustion systems [9,31]. In some cases, the transport of materials is accomplished by making a slurry of the solid particles in a liquid and pumping the mixture through a pipe. Liquid–liquid mixtures are encountered when dealing with emulsions as well as in liquid–liquid extraction. An example could be two-phase flow that can occur under normal and accidental conditions in various processes such as heat exchange, steam power generation, and oil or natural gas pumping systems. Another example is the flow of two immiscible liquids in pipelines that are of

* Corresponding author. Tel.: +82 64 754 3664; fax: +82 64 756 1745.
E-mail address: kyungyk@cheju.ac.kr (K.Y. Kim).

0021-9991/$ - see front matter © 2008 Published by Elsevier Inc.
doi:10.1016/j.jcp.2007.12.025

particular interest in many engineering applications. As a typical example, liquid hydrocarbons transported in pipelines over a long distance (for example, crude oil, gasoline, diesel) often contain free water [5]. Knowledge of the binary mixture flow is important in the design and operation of such systems. As the heterogeneous phase affects the safety, control, operation, and optimization of the process, it is important to know the phase boundaries online without disturbing the flow fields. For the visualization of two-phase flow, various tomography techniques with noninvasive and nonintrusive characteristics have been developed, for example, gamma densitometry [32], ultrasonic imaging [44] and nuclear magnetic resonance imaging [7]. Electrical impedance tomography (EIT) [29,43] has been used quite often in the medical field, as an alternative to X-ray imaging, computerizied tomography (CT), gamma camera, magnetic resonance imaging (MRI) and ultrasound tomography (UST). Some of these techniques are expensive and even cause adverse health effects. EIT, therefore, has been employed to investigate two-phase flow phenomena [11], because it is relatively inexpensive and has good temporal resolution. However, it suffers from poor spatial resolution as it has diffusive and soft-field characteristics and this needs to be improved. At the same time, the data acquisition time in EIT is fast which makes it more suitable for fast transient processes.

Image reconstruction in EIT is a kind of nonlinear optimization problem in which the solution is obtained iteratively through forward and inverse solvers. The physical relationship between the internal conductivity and surface voltages is governed by a partial differential equation with an appropriate boundary condition. It is, in most cases, impossible to obtain an analytical solution for the forward problem so that a numerical technique such as the finite element method (FEM) is employed. Reconstruction algorithms for EIT can be classified into two categories. Firstly, the so-called 'static imaging techniques' are used for the case where the internal conductivity of the body is time invariant within the time taken to acquire a full set of measurement data [45]. Therefore, these static imaging techniques often fail when there are fast impedance changes. In the other category, there are the so-called 'dynamic imaging techniques', which have been introduced to enhance the temporal resolution for situations where the conductivity distribution inside the body changes rapidly. In these dynamic approaches, the temporal resolution can be improved by a factor of p (p is the number of current patterns in a conventional frame). The reduction in current patterns is also made possible by the analysis of current patterns to use only the optimal current patterns in a dynamic scenario. With regard to optimal current patterns, Isaacson [10] showed that the best current patterns to distinguish a central concentric inhomogeneity inside an otherwise homogeneous circular conductor are trigonometric current patterns. Gisser et al. [6] compared the distinguishabilities by using adjacent, opposite and cosine current patterns on a circular conductor model without a centered circular target and showed that the maximum cosine current equal to the current injected with the opposite or the adjacent electrode is the optimum current pattern. Newell et al. [30] showed that cosine current patterns can distinguish smaller inhomogeneities as compared to when opposite and adjacent current patterns are used. It is generally known that opposite current patterns are optimal if the total current (sum of the amplitude of injected currents) is kept constant and trigonometric current patterns are optimum if the maximum of the injected current is kept constant. With or without using the optimal current patterns (usually, the first two modes of cosine and sine patterns), many dynamic techniques were developed, in which the inverse problem is treated as a nonlinear state estimation problem in which the time-varying state is estimated with the aid of a linearized Kalman filter (LKF) [39,41], extended Kalman filter (EKF) [15], and interacting multiple model (IMM) that uses multiple EKFs [16,18]. The state evolution model used in these dynamical approaches is the random-walk model in which the rate of evolution is governed by the covariance of the process noise. However, the modelling uncertainty of the random-walk model may be large enough to cause significant negative effects on the quality of the reconstructed image.

Having laid the foundation for two-phase flow estimation and dynamic imaging, a special class of EIT inverse problems is discussed hereafter, in which the position and shape of the objects in the domains are unknown and to be identified, while the conductivities of these objects are known *a priori*. There are two types of such problems for binary mixtures according to the topology of the boundary to be estimated: open boundary problems in which the object domain can be divided into two disjoint regions which are separated by an open boundary [3,4,24,27,34–37]; and closed boundary problems, in which the anomalies are enclosed by the background substance and which are used in this study.

It is also worth mentioning that the boundary detection could also be considered using the well-known level-set methods. The level-set method was first proposed by Osher and Sethian [46] for tracing interfaces

between different phases of fluid flows. Rondi and Santosa [47] applied and analyzed phase-filed methods to the reconstruction of piecewise constant conductivities in EIT. Following the work on level sets in [48–50], a method based on level-set method is proposed in [4] to solve the inverse problem arising from EIT by minimizing the L^2-norm of the difference between the potential and measured voltage and by incorporating total variational regularization. In [51], results are shown from a narrow-band level-set method applied to 2D and 3D EIT incorporating limited angle ultrasound time of flight data which is reported as an improvement over [52] that considers EIT only. The narrow-band technique for calculating Jacobian results in computationally efficient and fast algorithm and in [53], application of EIT for cryosurgery monitoring is considered in which the cancerous tissue is treated by local freezing technique using a small needle-like cryosurgery probe and the interface between the frozen and non frozen tissue is monitored using level-set method. In [54], the level-set regularization is considered for EIT and Gauss–Newton methods are applied. In general, using an iterative method with an update formula for level-set functions, the interface between two materials can be recovered well in the domain of EIT. Although, level-set method was initially introduced for tracking propagating boundaries, they are generally used for tracking static interfaces for the reason that they are slow, i.e., the computational cost is very high as they need many iterations (hundreds of nonlinear steps). So, it is desirable to have a cost-effective inverse algorithm which not only tracks dynamic interfaces, but can also handle higher level of noise in the measurement and requires less measurement data. Therefore, the Kalman-type reconstruction algorithms serve this purpose as they are modelled on a Markov chain and traditionally built on linear operators perturbed by Gaussian noise. Since, image reconstruction in EIT is a nonlinear problem, therefore, the nonlinear version of Kalman-type filters should be considered.

In context of the boundary representation scheme used in this paper, Han and Prosperetti [8] considered a shape decomposition technique based on the boundary element method, where the boundary of each target was represented in terms of Fourier coefficients rather than a point-wise discretization. Kolehmainen et al. [25] developed an algorithm to recover the region boundaries of piecewise constant coefficients of an elliptic partial differential equation (PDE) from boundary data for the application to optical tomography, which is also applicable to EIT [19]. For an optimal solution of the Fourier coefficients, a Newton-type method is employed, which is usually time consuming although it shows good performance in many optimization problems. However, its down side is the slow convergence which has an adverse effect in the application to mixture flows undergoing fast transient. Jeon et al. [14] estimated the Fourier coefficients with the use of a multi-layered neural network (MNN) because of its conceptual simplicity, fast online calculation, ease of implementation, ability to control the compromise between the noise treatment and spatial resolution and most importantly, it does not require linearization of the problem (use of first derivative i.e, Jacobian). The neural network used was backpropagation neural network which is regarded as a universal approximator. At the same time, Kim et al. [17] used the exact expression of Jacobian and tested it successfully with experimental data. Kim et al. [21] improves the performance by considering weighted multi-layered neural networks, each working together with a different sigmoid function. Since the higher modes of Fourier coefficients are more sensitive to noise so Kim et al. [22] proposed the use of front points in polar coordinates to estimate the closed boundary. The proposed scheme lacked analytical Jacobian and perturbation method was used to estimate the Jacobian matrix. Because of a lack of Jacobian, Kim et al. [23] used the WMNN to estimate the front points. Most recently, Kim et al. [20] used IMM to estimate the Fourier coefficients by considering multiple EKFs, each working on a different measurement noise model. So far, the only experimental results available are for static cases in closed boundary representation.

EKF is the most widely used dynamic estimation algorithm for nonlinear systems. However, it is difficult to tune, and is only reliable for systems that are almost linear on the time scale of the updates. To overcome these difficulties, the unscented transform (UT) was developed by Julier and Uhlmann [12,13] as a method to propagate mean and covariance information through a nonlinear transformation. It is more accurate, easier to implement, and uses the same order of calculations as linearization. Also, the linearization in EKF is possible only if the Jacobian matrix exists. However, this is not always the case. Some systems contain discontinuities in process model, and in another cases, the Jacobian matrices can be very difficult and error-prone process and in most cases introduce human coding errors that undermine the performance. Therefore, in this paper, the UKF is used to estimate the nonstationary phase boundaries represented by truncated Fourier coefficients and does not require the use of the Jacobian matrix. UKF is feasible here as there are less shape parameters

to estimate than the conductivity profile (which will be explained in the ensuing sections). Numerical and experimental results are also provided to evaluate the performance of UKF over EKF.

2. Mathematical formulation

2.1. Finite element formulation of the forward problem

The numerical model used in this work is based on EIDORS [42]. The finite element model to solve the EIT problem can be found in [25,39]. However, the finite element approximation will be described briefly to formulate the inverse solution.

When electrical currents I_l $(l = 1,2,\ldots,L)$ are injected into a body $\Omega \in R^2$ through the electrodes e_l $(l = 1,2,\ldots,L)$ attached on the boundary $\partial\Omega$, and the conductivity distribution $\sigma(x,y)$ is known for Ω, the corresponding electrical potential $u(x,y)$ on Ω can be determined uniquely from a partial differential equation, which can be derived from the Maxwell equations:

$$\nabla \cdot (\sigma \nabla u) = 0 \quad \text{in } \Omega \tag{1}$$

with the following boundary conditions based on the complete electrode model:

$$u + z_l \sigma \frac{\partial u}{\partial n} = U_l \quad \text{on } e_l, \quad l = 1,2,\ldots,L, \tag{2}$$

$$\int_{e_l} \sigma \frac{\partial u}{\partial n} \mathrm{d}S = I_l, \quad l = 1,2,\ldots,L, \tag{3}$$

$$\sigma \frac{\partial u}{\partial n} = 0 \quad \text{on } \partial\Omega \setminus \bigcup_{l=1}^{L} e_l, \tag{4}$$

where z_l is the effective contact impedance between the lth electrode and electrolyte, U_l is the potential on the lth electrode, e_l, n is the outward unit normal and L is the number of electrodes. Various forms of boundary conditions may be used in the forward model. We have chosen the complete electrode model (CEM) which takes into account the discrete electrodes, effects of the contact impedance and the shunting effect of the electrodes. In addition, the following two constraints for the injected currents and measured voltages ensure the existence and uniqueness of the solution:

$$\sum_{l=1}^{L} I_l = 0, \tag{5}$$

$$\sum_{l=1}^{L} U_l = 0. \tag{6}$$

In the context of FEM, the object area is discretized into sufficiently small triangular elements having a node at each corner and it is assumed that the resistivity distribution is constant within each element. Let N be the number of nodes in the finite element mesh. The potential distribution u within the object is approximated as

$$u \simeq u^h(x,y) = \sum_{i=1}^{N} \alpha_i \varphi_i(x,y) \tag{7}$$

and the potential on the electrodes is represented by

$$U^h = \sum_{j=1}^{L-1} \beta_j \mathbf{n}_j, \tag{8}$$

where the function φ_i is the two-dimensional first-order basis function and the basis for the measurements are $\mathbf{n}_1 = [1,-1,0,\ldots,0]^{\mathrm{T}}$, $\mathbf{n}_2 = [1,0,-1,\ldots,0]^{\mathrm{T}} \in R^{L\times 1}$, etc. In this α_i and β_i are the coefficients to be determined.

The following set of linear equations is obtained from finite element formulation:

$$\mathbf{Ab} = \widetilde{\mathbf{I}}, \tag{9}$$

where

$$\mathbf{A} = \begin{pmatrix} \mathbf{B} & \mathbf{C} \\ \mathbf{C}^{\mathrm{T}} & \mathbf{D} \end{pmatrix}, \quad \mathbf{b} = \begin{pmatrix} \boldsymbol{\alpha} \\ \boldsymbol{\beta} \end{pmatrix}, \quad \text{and} \quad \widetilde{\mathbf{I}} = \begin{pmatrix} \mathbf{0} \\ \boldsymbol{\zeta} \end{pmatrix}, \tag{10}$$

where $\boldsymbol{\alpha} = (\alpha_1, \ldots, \alpha_N)^{\mathrm{T}} \in R^{N\times 1}$, $\boldsymbol{\beta} = (\beta_1, \ldots, \beta_{L-1})^{\mathrm{T}} \in R^{L-1}$ and $\mathbf{0} \in R^{N\times 1}$. The reduced current vector $\zeta = (I_1 - I_2, I_1 - I_3, \ldots, I_1 - I_L)^{\mathrm{T}} \in \mathrm{R}^{(L-1)\times 1}$, and the stiffness matrix $\mathbf{A}$ is of the form

$$\mathbf{B}(i,j) = \int_{\Omega} \sigma \nabla \varphi_i . \nabla \varphi_j \, \mathrm{d}r + \sum_{l=1}^{L} \frac{1}{z_l} \int_{e_l} \varphi_i \varphi_j \, \mathrm{d}S, \quad i,j = 1,2,\ldots,N, \tag{11}$$

$$\mathbf{C}(i,j) = -\left(\frac{1}{z_l} \int_{e_1} \varphi_i \, \mathrm{d}S - \frac{1}{z_{j+1}} \int_{e_{j+1}} \varphi_i \, \mathrm{d}S \right), \quad \begin{matrix} i = 1,2,\ldots,N, \\ j = 1,2,\ldots,L-1, \end{matrix} \tag{12}$$

$$\mathbf{D}(i,j) = \begin{cases} \frac{|e_1|}{z_1}, & i \neq j, \\ \frac{|e_1|}{z_1} + \frac{|e_{j+1}|}{z_{j+1}}, & i = j, \end{cases} \quad i,j = 1,2,\ldots,L-1, \tag{13}$$

where $|e_j|$ is the width of the electrode j.

2.2. Boundary expression

In this paper, we consider the recovery of sufficiently smooth region boundaries. The assumption made is that the conductivity values are known *a priori*, but the information about the geometry and shape is missing. This leads to a nonlinear and ill-posed inverse problem in which the coefficients representing the boundary shape are to be estimated. Therefore, the forward solver has to be modified as a set of coefficients representing the boundary shapes to the data on $\partial\Omega$.

Lets assume that the region Ω is divided into disjoint, simply connected domains A_k

$$\Omega = \bigcup_{k=0}^{P} A_k, \tag{14}$$

where P regions exist in closed boundary representation as shown in Fig. 1. Assuming the region boundaries in closed boundary strategy represented by C_k, we can then denote by $\chi_k(r)$ the characteristic function of subregion A_k, we can write

$$\sigma = \sum_{k=0}^{P} \sigma_k \chi_k(r). \tag{15}$$

By substituting (15) into (11), we obtain

$$\mathbf{B}(i,j) = \sum_{k=0}^{P} \int_{\mathrm{supp}(\varphi_i \varphi_j) \cap A_k} \sigma_k \nabla \varphi_i \nabla \varphi_j \, \mathrm{d}r + \sum_{l=1}^{L} \frac{1}{z_l} \int_{e_l} \varphi_i \varphi_j \, \mathrm{d}S, \tag{16}$$

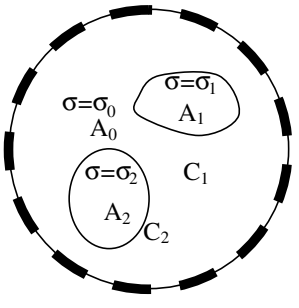

Fig. 1. Examples of smooth region boundaries.

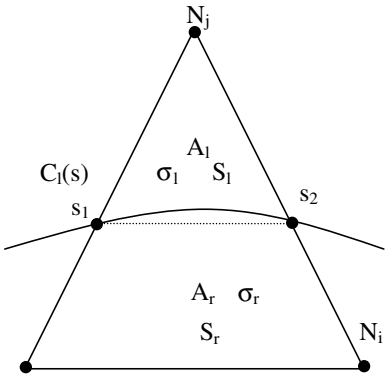

Fig. 2. Assignment of conductivity to mesh crossing elements.

where supp($\varphi_i\varphi_j$) is a part of domain Ω where both the basis functions φ_i and φ_j are non-zero. The implementation of the integrals of the form (16) has been described previously in [25,34].

In the first step, mesh elements Ω_m are classified into sets of elements inside the region A_k ($k = 0, 1$) and into set of elements intercepted by the boundary C_k. For the elements that lie in the region A_k, they are assigned their corresponding conductivity values σ_k, however, for the elements that lie on the boundary C_k, the area weighted conductivity (Figs. 2 and 3) values are assigned as [25]

$$\sigma_e = \frac{\sigma_l S_l + \sigma_r S_r}{S_e (= S_l + S_r)}, \tag{17}$$

where S_l and S_r denotes the area.

We assume that the outer boundary of the body, that is, $\partial\Omega$ is known. If phase boundaries of the objects are sufficiently smooth, they can be approximated in the form

$$C_l(s) = \begin{pmatrix} x_l(s) \\ y_l(s) \end{pmatrix} = \sum_{n=1}^{N_\theta} \begin{pmatrix} \gamma_n^{x_l} \theta_n^x(s) \\ \gamma_n^{y_l} \theta_n^y(s) \end{pmatrix}, \tag{18}$$

where $C_l(s)$ ($l = 1,2, \ldots, S$) is the boundary of the lth object, S is the number of objects in the body, $\theta_n(s)$ are periodic and differentiable basis functions and N_θ is the number of basis functions (three for elliptic objects). In this paper, we express the phase boundaries as Fourier series in two-dimensional coordinates with respect to parameter s, that is, we use the basis functions of the form

$$\theta_1^\alpha(s) = 1, \tag{19}$$

$$\theta_n^x(s) = \sin(2\pi \frac{n}{2} s), \quad n = 2, 4, 6, \ldots, N_\theta - 1, \tag{20}$$

$$\theta_n^y(s) = \cos(2\pi \frac{(n-1)}{2} s), \quad n = 1, 3, 5, \ldots, N_\theta, \tag{21}$$

where $s \in [0, 1]$ and α denotes either x or y. The boundaries are identified with the vector γ of the shape coefficients, that is,

$$\gamma = (\gamma_1^{x_1}, \ldots, \gamma_{N_\theta}^{x_1}, \gamma_1^{y_1}, \ldots, \gamma_{N_\theta}^{y_1}, \ldots, \ldots, \gamma_1^{x_s}, \ldots, \gamma_{N_\theta}^{x_s}, \gamma_1^{y_s}, \ldots, \gamma_{N_\theta}^{y_s})^{\mathrm{T}}, \tag{22}$$

where $\gamma \in R^{2SN_\theta \times 1}$.

2.3. Inverse solver based on unscented Kalman filter

Before discussing UKF, it is essential to discuss EKF and pinpoint its flaws. The EKF has become a standard technique used in a number of nonlinear estimation and machine learning applications, e.g. estimating the state of nonlinear dynamic system, estimating parameters for nonlinear system identification (learning weights of a neural network) and dual estimation (Expectation Maximization (EM) algorithm) where both states and

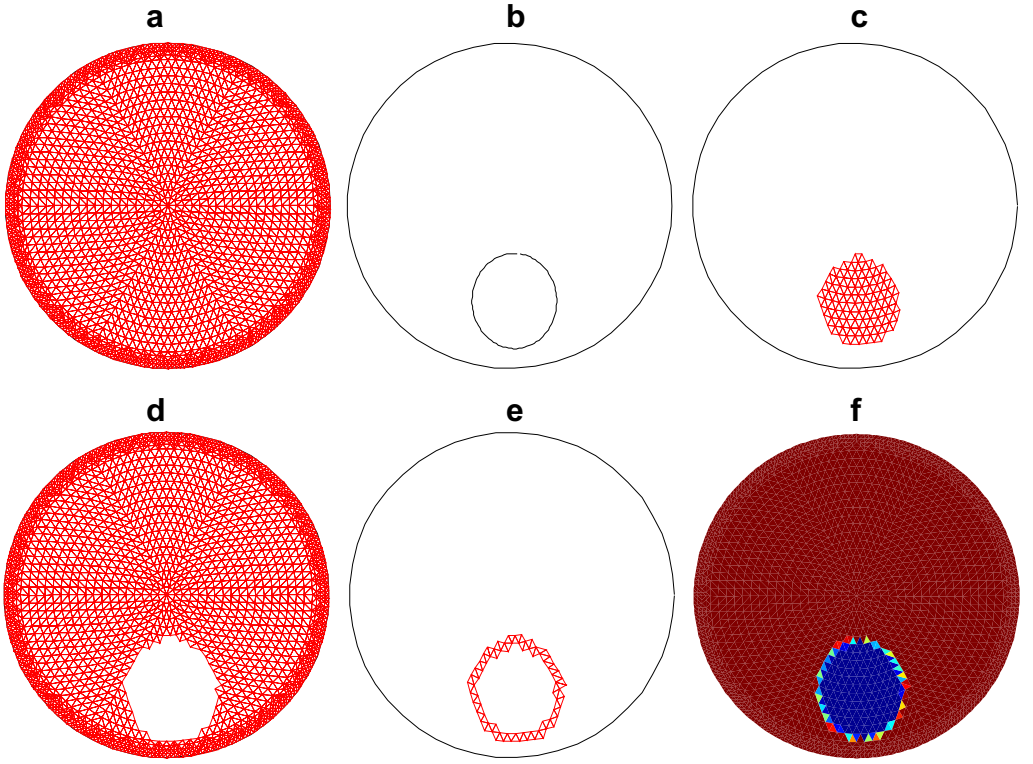

Fig. 3. Fourier coefficient to underlying conductivity profiles: (a) FEM discretization of the domain; (b) boundary represented by Fourier coefficient; (c) mesh elements belonging to target are assigned σ_i; (d) mesh elements belonging to the background are assigned σ_r; (e) mesh elements lying on the interface are assigned area average conductivity values assigned using Eq. (17); and (f) final conductivity values at the end of assignment.

parameters are estimated simultaneously. However, in EKF, the state distribution is approximated by a Gaussian random variable (GRV), which is then propagated analytically through the first-order linearization of the nonlinear system. This can introduce large errors in the true posterior mean and covariance of the transformed

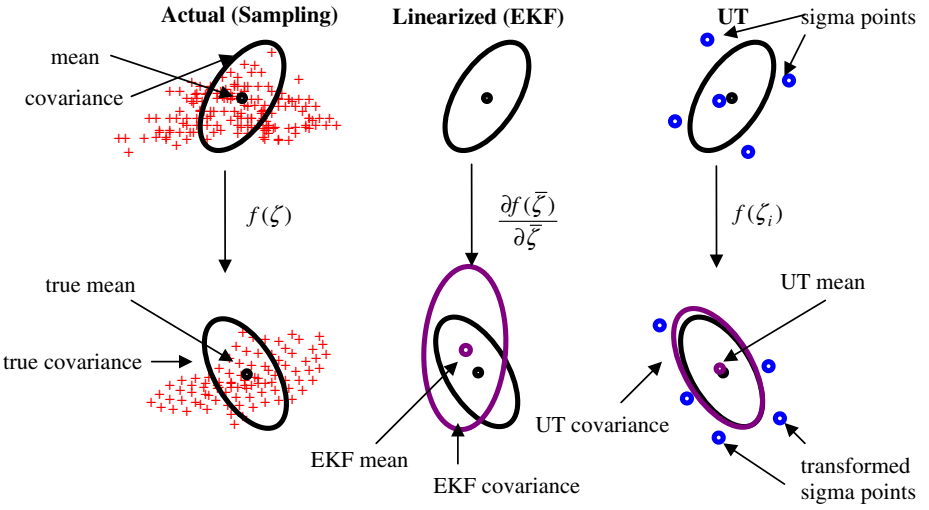

Fig. 4. An example of unscented transform for mean and covariance propagation: (a) actual; (b) first-order linearization (EKF); and (c) unscented transform.

GRV (see Fig. 4), which may lead to suboptimal performance and sometimes divergence of the filter. The UKF addresses this problem by carefully choosing sample points instead of GRV, and which when propagated through the true nonlinear system, captures the posterior mean and covariance accurately to the 3rd order (Taylor series expansion) for any nonlinearity. The EKF, in contrast, only achieves first-order accuracy. Remarkably, the computational complexity of the UKF is the same order as that of EKF as mentioned in [13].

Given the linear state equation and nonlinear measurement equation [20]

$$\gamma_k = \mathbf{I} \cdot \gamma_{k-1} + \omega_{k-1}, \tag{23}$$

$$U_k = h_k(\gamma_k) + \upsilon_k, \tag{24}$$

where $\omega_k \in R^{N\times 1}$ and $\upsilon_k \in R^{L\times 1}$ are assumed to be white Gaussian noise with covariance $\mathbf{Q} = E[\omega_k \omega_k^{\mathrm{T}}]$ and $\mathbf{R} = E[\upsilon_k \upsilon_k^{\mathrm{T}}]$ respectively. Also, $h_k(\gamma_k)$ is the forward solver to obtain boundary voltage.

Given, the stochastic nonlinear state-space model, the unscented Kalman filter algorithm [13] is as follows:

Initialize with:

$$\hat{\gamma}_0 = E[\gamma_0], \tag{25}$$

$$\mathbf{P}_0 = E[(\gamma_0 - \hat{\gamma}_0)(\gamma_0 - \hat{\gamma}_0)^{\mathrm{T}}], \tag{26}$$

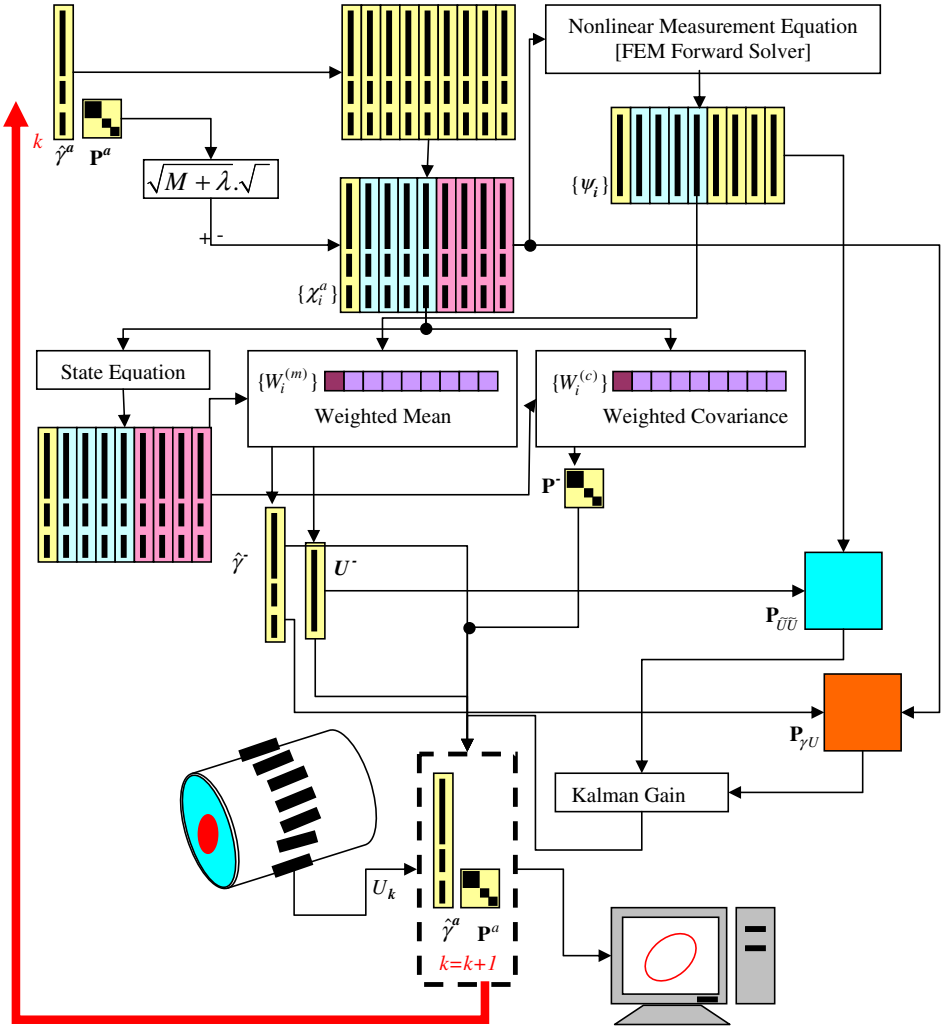

Fig. 5. Block diagram of the UKF for phase boundary estimation in EIT.

$$\hat{\gamma}_0^a = E[\gamma^a] = [\hat{\gamma}_0^{\mathrm{T}} \quad 0 \quad 0]^{\mathrm{T}}, \tag{27}$$

$$\mathbf{P}_0^a = E[(\gamma_0^a - \hat{\gamma}_0^a)(\gamma_0^a - \hat{\gamma}_0^a)^{\mathrm{T}}] = \begin{bmatrix} \mathbf{P}_0 & 0 & 0 \\ 0 & \mathbf{Q} & 0 \\ 0 & 0 & \mathbf{R} \end{bmatrix} \tag{28}$$

for $k \in \{1, \ldots, \infty\}$.

Calculate sigma points:

$$\chi_{k-1}^a = \left[\hat{\gamma}_{k-1}^a \quad \hat{\gamma}_{k-1}^a + \sqrt{(M+\lambda)\mathbf{P}_{k-1}^a} \quad \hat{\gamma}_{k-1}^a - \sqrt{(M+\lambda)\mathbf{P}_{k-1}^a}\right]. \tag{29}$$

Time update:

$$\chi_{k|k-1}^{\gamma} = \mathbf{I} \cdot \chi_{k-1}^{\gamma} + \chi_{k-1}^{\omega}, \tag{30}$$

$$\hat{\gamma}_k^- = \sum_{i=0}^{2M} W_i^{(m)} \chi_{i,k|k-1}^{\gamma}, \tag{31}$$

$$\mathbf{P}_k^- = \sum_{i=0}^{2M} W_i^{(c)} [\chi_{i,k|k-1}^{\gamma} - \hat{\gamma}_k^-][\chi_{i,k|k-1}^{\gamma} - \hat{\gamma}_k^-]^{\mathrm{T}}, \tag{32}$$

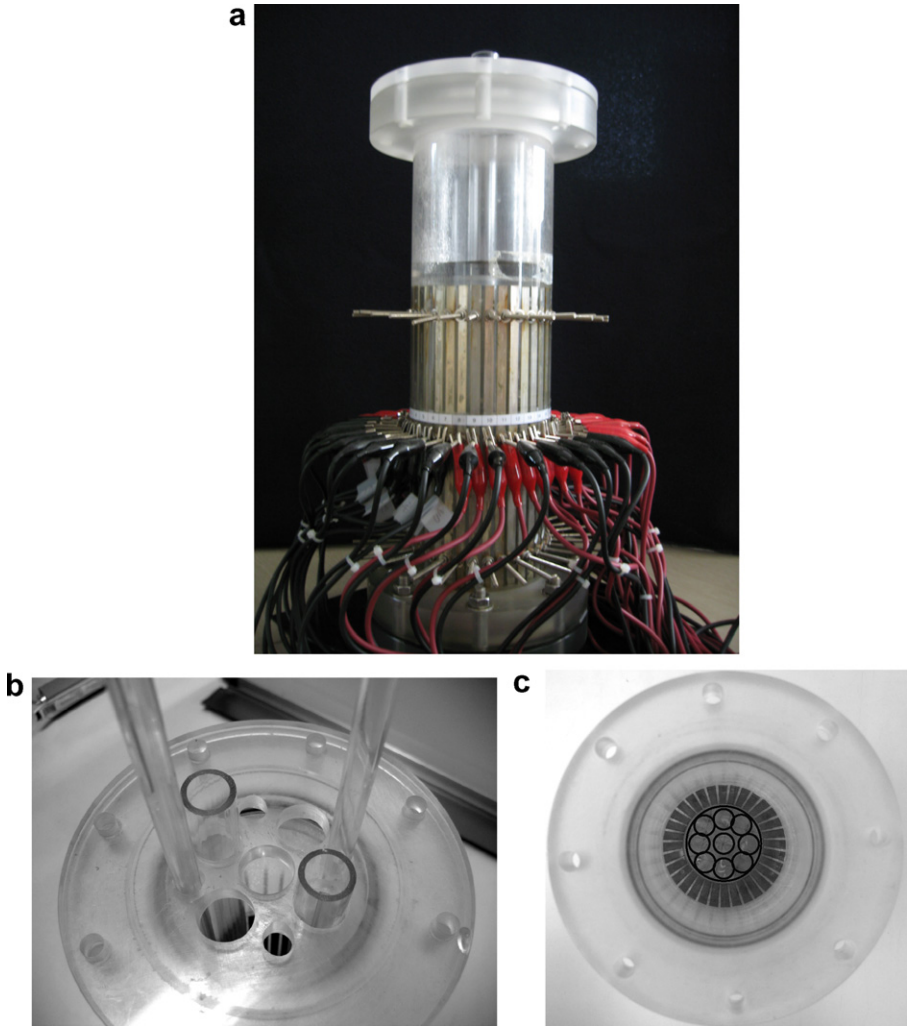

Fig. 6. Experimental setup: (a) phantom; (b) plastic rods used as targets; and (c) positions where the plastic targets could be placed.

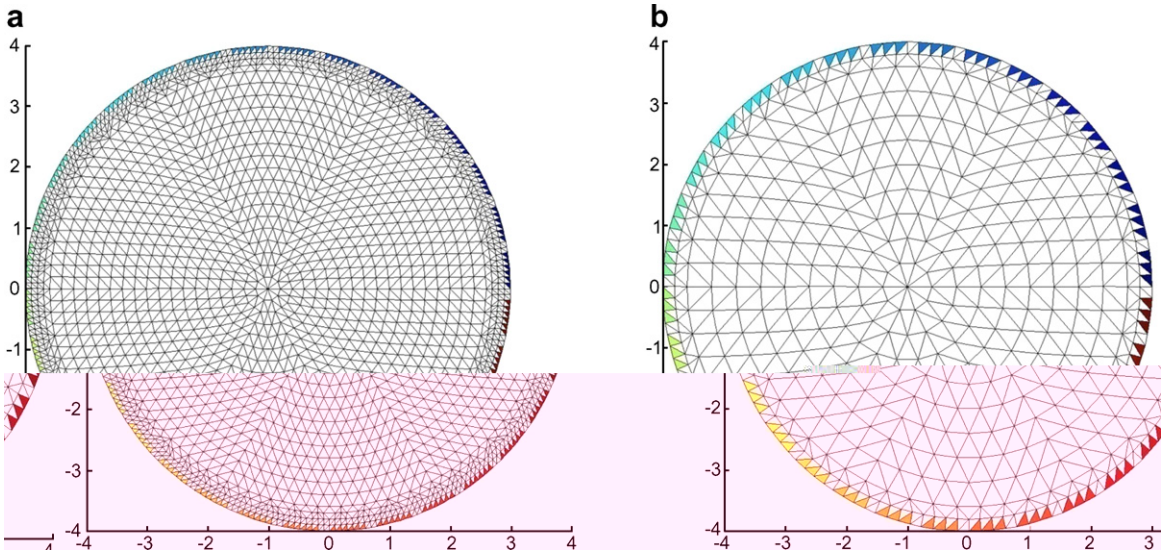

Fig. 7. Meshes used in: (a) forward solver; and (b) inverse solver.

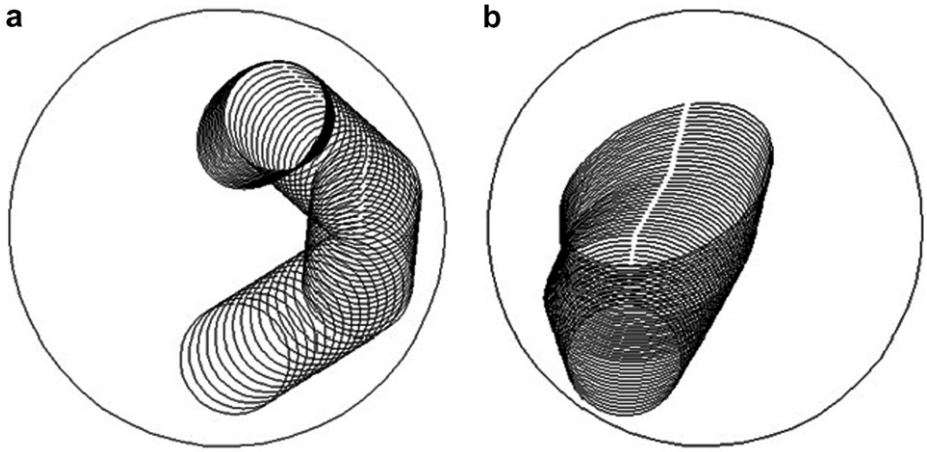

Fig. 8. Evolution model for numerical simulations: (a) scenario 1; and (b) scenario 2.

Table 1
Parameters used in simulations for scenario 1

Parameters	EKF			UKF		
	1% White Gaussian noise	2% White Gaussian noise	3% White Gaussian noise	1% White Gaussian noise	2% White Gaussian noise	3% White Gaussian noise
$\mathbf{Q}$	$0.01\boldsymbol{I}_N$	$0.01\boldsymbol{I}_N$	$0.01\boldsymbol{I}_N$	$0.01\boldsymbol{I}_N$	$0.01\boldsymbol{I}_N$	$0.01\boldsymbol{I}_N$
$\mathbf{R}$	$200\boldsymbol{I}_L$	$900\boldsymbol{I}_L$	$3000\boldsymbol{I}_L$	$10\boldsymbol{I}_L$	$90\boldsymbol{I}_L$	$300\boldsymbol{I}_L$
$\mathbf{P}_0$	$0.1\boldsymbol{I}_N$	$0.1\boldsymbol{I}_N$	$0.1\boldsymbol{I}_N$	$0.1\boldsymbol{I}_N$	$0.1\boldsymbol{I}_N$	$0.1\boldsymbol{I}_N$
$\bar{\alpha}$	0.001	0.01	0.1	–	–	–
α	–	–	–	0.1	0.08	0.2
β	–	–	–	2	2	2
κ	–	–	–	0	0	0

$$\psi_{k|k-1} = h_k(\chi^{\gamma}_{k|k-1}) + \chi^{v}_{k-1}, \tag{33}$$

$$\widehat{U}^{-}_{k} = \sum_{i=0}^{2M} W^{(m)}_{i} \psi_{i,k|k-1}. \tag{34}$$

Measurement update:

$$\mathbf{P}_{\widetilde{U}_k \widetilde{U}_k} = \sum_{i=0}^{2M} W^{(c)}_{i} [\psi_{i,k|k-1} - \widehat{U}^{-}_{k}][\psi_{i,k|k-1} - \widehat{U}^{-}_{k}]^{\mathrm{T}}, \tag{35}$$

$$\mathbf{P}_{\gamma_k U_k} = \sum_{i=0}^{2M} W^{(c)}_{i} [\chi^{\gamma}_{i,k|k-1} - \hat{\gamma}^{-}_{k}][\chi^{\gamma}_{i,k|k-1} - \hat{\gamma}^{-}_{k}]^{\mathrm{T}}, \tag{36}$$

$$\mathbf{K}_k = \mathbf{P}_{\gamma_k U_k} \mathbf{P}^{-1}_{\widetilde{U}_k \widetilde{U}_k}, \tag{37}$$

$$\hat{\gamma}_k = \hat{\gamma}^{-}_{k} + \mathbf{K}_k (U_k - \widehat{U}^{-}_{k}), \tag{38}$$

$$\mathbf{P}_k = \mathbf{P}^{-}_{k} - \mathbf{K}_k \mathbf{P}_{\widetilde{U}_k \widetilde{U}_k} \mathbf{K}^{\mathrm{T}}_{k}, \tag{39}$$

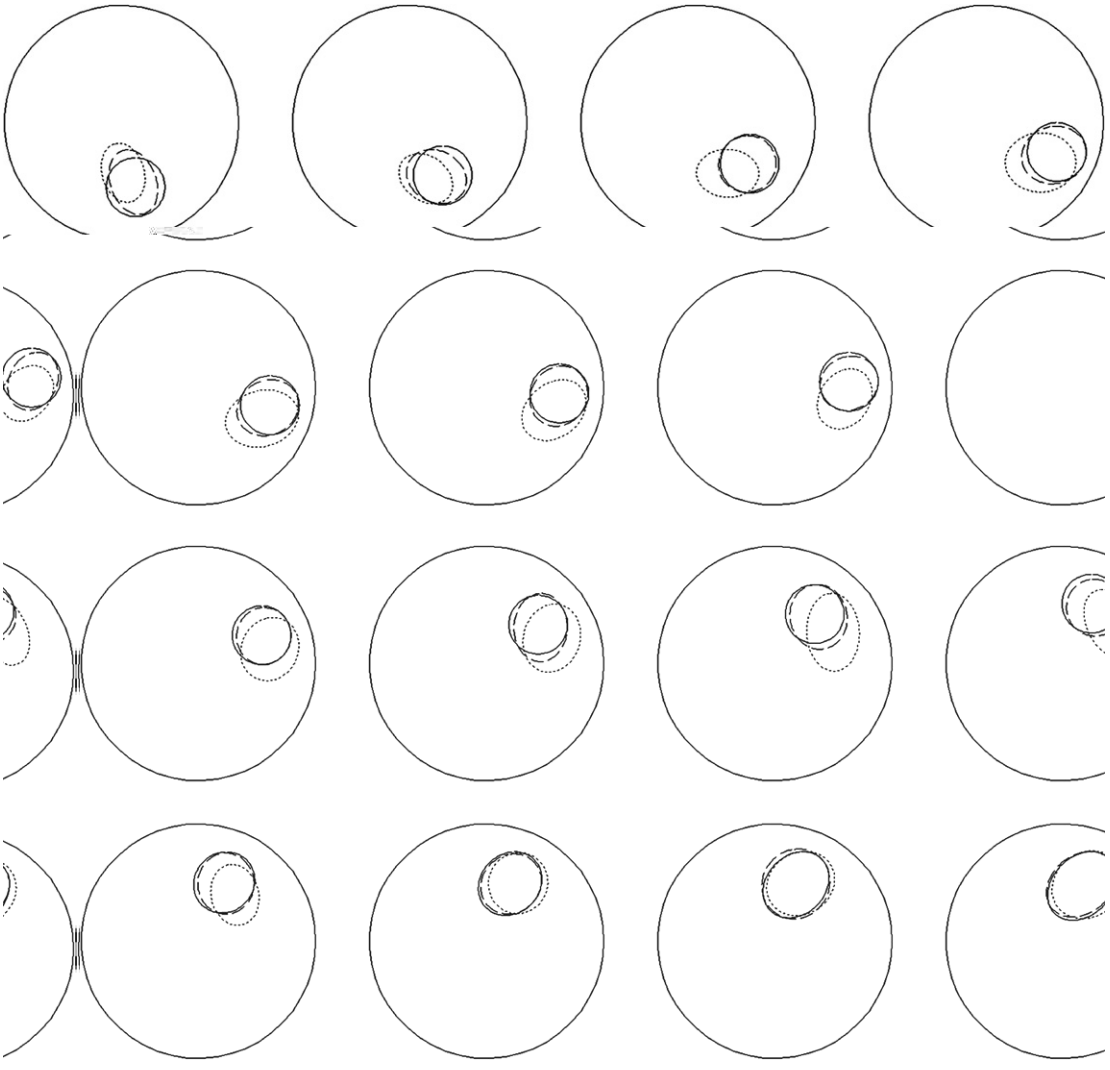

Fig. 9. Reconstructed boundaries for scenario 1 with measurements perturbed by 1% white Gaussian noise. Solid line, dotted line and dashed line represent the true boundary, boundary estimated by EKF, and boundary estimated by UKF, respectively.

where $\gamma^a = [\gamma^{\mathrm{T}} \quad \omega^{\mathrm{T}} \quad \upsilon^{\mathrm{T}}]^{\mathrm{T}}$, $\chi^a = [(\chi^{\gamma})^{\mathrm{T}} \quad (\chi^{\omega})^{\mathrm{T}} \quad (\chi^{\upsilon})^{\mathrm{T}}]^{\mathrm{T}}$, $\lambda = \alpha^2(M+\kappa) - M$ is composite scaling parameter, α determines the spread of sigma points (is usually set to a small positive value e.g. $1 \leqslant \alpha \leqslant 10^{-4}$). The κ is secondary scaling parameter (is usually set to 0 or $3 - M$) and β is used to incorporate prior knowledge of the distribution of γ (for Gaussian distribution, $\beta = 2$ is optimal). Weights W_i are given by

$$W_0^{(m)} = \lambda/(M+\lambda), \tag{40}$$

$$W_0^{(c)} = \lambda/(M+\lambda) + (1-\alpha^2+\beta), \tag{41}$$

$$W_i^{(m)} = W_i^{(c)} = 1/\{2(M+\lambda)\}, \quad i = 1, \ldots, 2M, \tag{42}$$

where $M = 2N + L$, N is the dimension of Fourier coefficients and L is the total number of electrodes. The above mentioned computational procedure to compute the Fourier coefficients is also explained in block diagram in Fig. 5. Here, the augmented state vector $\hat{\gamma}^a$ and the augmented covariance matrix $\mathbf{P}^a$ is updated when the voltage measurement U_k becomes available at kth iteration. Two significant covariance matrices shown in Fig. 5 are $\mathbf{P}_{\underset{U\,U}{\sim\sim}}$ and $\mathbf{P}_{\gamma U}$. During the iterative process $\mathbf{P}_{\underset{U\,U}{\sim\sim}}$ will be reduced so that the transformed sigma points (also putting Fig. 4 in perspective) move towards the cluster mean. With the introduction of the measurement data U_k, the cluster mean will then move further towards the true mean and as a consequence $\mathbf{P}_{\gamma U}$ will be reduced. Here, it should be noted that if the target is static during the application of some current patterns then the transformed sigma points will move towards the true mean and then spread again whenever the target changes its position. Therefore, the trade-off from performance standpoint is how many current patterns should be used and how fast should be the dynamic changes for UKF to capture them.

This method significantly differs from general Monte Carlo sampling methods which require more sample points in an attempt to propagate an accurate (possibly non-Gaussian) distribution of state. The UKF results in approximations that are accurate to the 3rd order for Gaussian inputs for all nonlinearities. For non-Gaussian inputs, approximations are accurate to at least the 2nd order, with the accuracy of third and higher-order moments determined by the choice of α and β in Eq. (41). The proof of this is provided in [13]. The UKF used in this study consists of an augmented state vector that contains both the process noise vector and the measurement noise vector. The reason behind taking the augmented state is to consider process and measurement noises with non-zero means. However, if the noise is additive and white Gaussian with zero mean, one can choose a much simpler form without taking the augmented state.

The complexity of UKF algorithm is M^3, where M is the dimension of augmented state. This has the same complexity as EKF. A number of other variations are also possible. For example, the matrix square root, which is implemented directly using a Cholesky factorization, is in general order $M^3/6$. However, the covari-

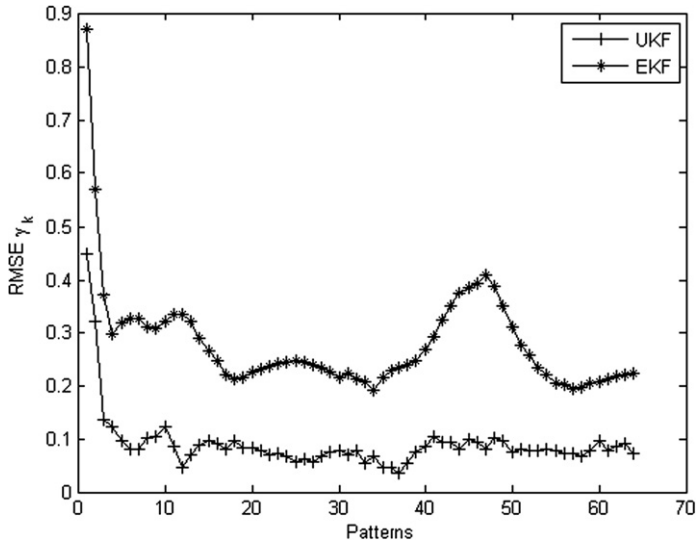

Fig. 10. RMSE comparison for scenario 1 with measurements perturbed by 1% white Gaussian noise.

ance matrices are expressed recursively, and thus the square root can be computed in the order $L \times M^2$ (L is the dimension of the voltage vector U) by performing a recursive update on the Cholesky factorization. Such kind of UKF is called square root UKF and its implementation is covered in [38]. For practical purposes, the alternatives are then to use the parallel implementation for sigma points calculation, to use limited measurement data, or to use the square root UKF with lower complexity.

3. Numerical and experimental results

To evaluate the performance of UKF, numerical and experimental studies were performed and the performance was assessed in comparison to extended Kalman filter (EKF) which is most often used as a dynamic inverse solver. The EKF uses Tikhonov regularization with regularization parameter $\bar{\alpha}$ and regularization matrix as identity matrix. The experimental setup shown in Fig. 6 consists of a circular phantom with a radius of 40 mm and a height of 80 mm was considered around which $L = 32$ electrodes (each of length 6 mm) were mounted. Two different meshes (Fig. 7) were used for forward (2121 nodes and 3984 elements) and inverse

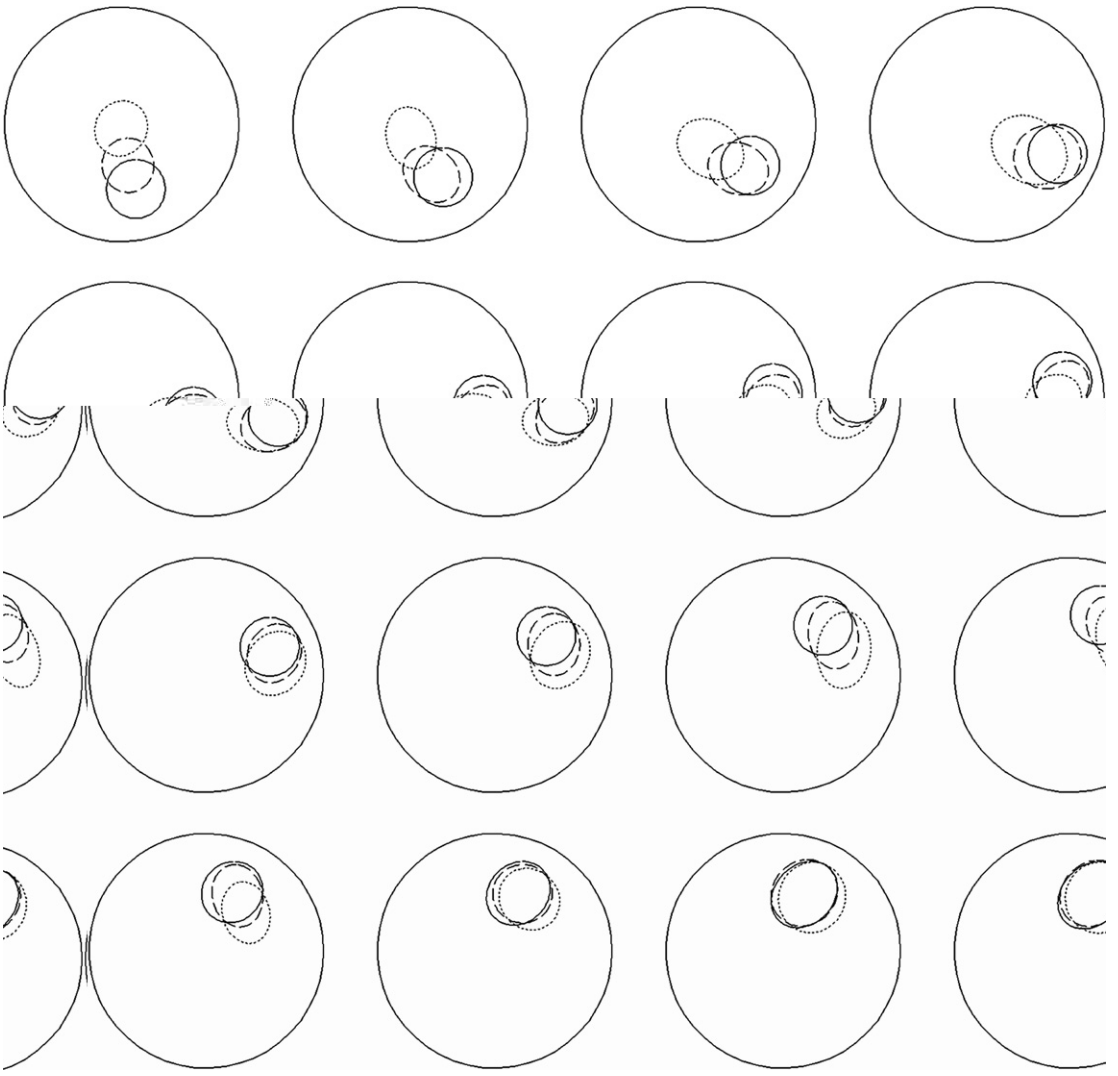

Fig. 11. Reconstructed boundaries for scenario 1 with measurements perturbed by 2% white Gaussian noise. Solid line, dotted line and dashed line represent the true boundary, boundary estimated by EKF, and boundary estimated by UKF, respectively.

solver (563 nodes and 993 elements) so that inverse crime is avoided in numerical simulations. As for the current injection protocol, opposite current patterns are used. Traditionally, for 32 electrodes' configuration, there are 16 opposite current patterns. However, since the goal of the current research is to use UKF in dynamic settings, a subset of opposite current patterns is considered in each image frame.

For numerical simulations, two scenarios are considered and their evolution models are shown in Fig. 8. In both scenarios, a very high contrast ratio between the background (330×10^9)and target (330) is maintained, as the final goal of this research is to model the boundaries of air bubbles in conducting liquids. Also, a total of $N = 6$ Fourier coefficients are reconstructed in the inverse solver that can represent an elliptic object and also meet the requirements of this study. In Fig. 8(a), in scenario 1, a circular target located in the south moves east at first and then towards north along the boundary until it stops just above the center. It then starts to expand and takes an elliptic shape. Here, a total of 64 image frames (a hypothetical number representing a frame in which the target remains static) are considered where each frame consists of one current pattern. i.e., target changes its position after every current pattern. Furthermore, the measurement data obtained is perturbed with 1%, 2% and 3% relative white Gaussian noise so as to emulate the real situations. The scenarios are then reconstructed with both EKF and UKF. As a performance metric, root mean square error (RMSE) is defined as,

$$\mathrm{RMSE}_{\gamma_k} = \frac{\|\gamma_{\mathrm{estimated},k} - \gamma_{\mathrm{true},k}\|}{\|\gamma_{\mathrm{true},k}\|}. \tag{43}$$

The parameters used in scenario 1 for both UKF and EKF are shown in Table 1. The reconstructed results and RMSE comparison are shown in Figs. 9–14. The reconstructed profiles in Figs. 9, 11 and 13 are shown after every four current patterns. For the case where measurement data is perturbed with 1% white Gaussian noise, it is noted that UKF is performing remarkably well in estimating the phase boundary. EKF, on the other hand, is trailing behind after application of each current pattern. However, it is noted that in the later part of the simulation, when the target is static and only expanding, the difference between UKF and EKF is a bit less. From the RMSE comparison for 1% white Gaussian noise case, it can be noted that on the average, the RMSE values for UKF are around 0.1 whereas for EKF, they are around 0.3. It can be established that a performance gain of three times is a marked improvement. Another key point is that UKF has a smaller transition period in the start as compared to EKF, and the difference in the transition periods between the two filters grows exponentially with the increase in measurement noise. Therefore, for 2% white Gaussian noise case, it can be seen in Fig. 12 that the first stable estimate for UKF is obtained around the 5th current pattern

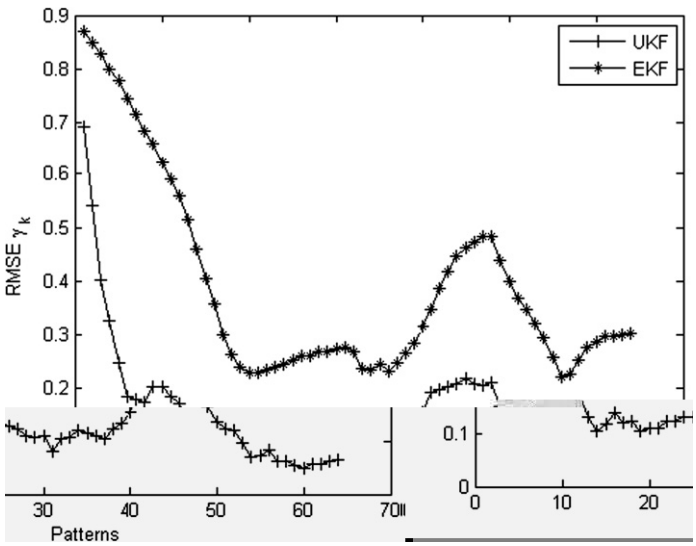

Fig. 12. RMSE comparison for scenario 1 with measurements perturbed by 2% white Gaussian noise.

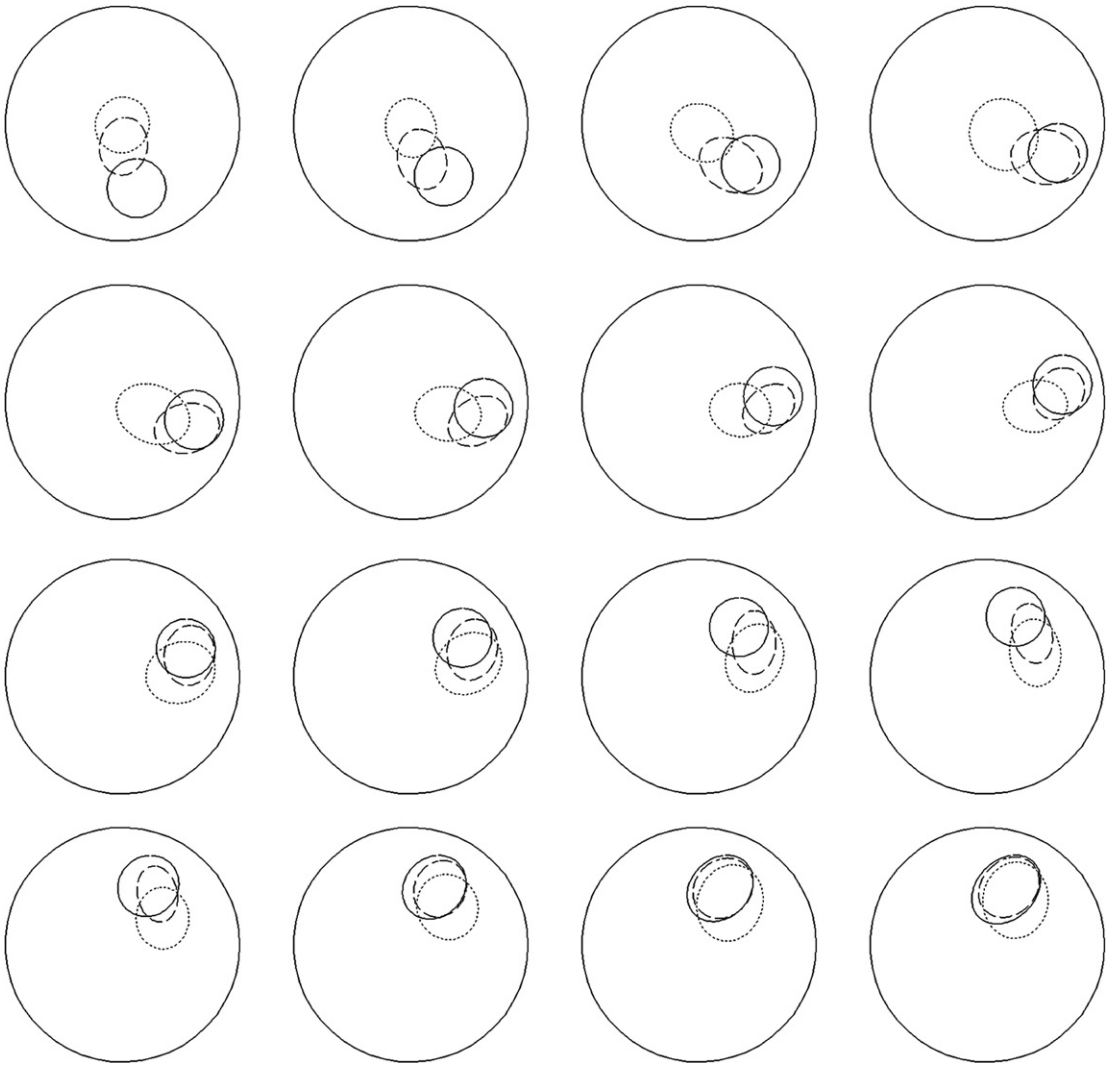

Fig. 13. Reconstructed boundaries for scenario 1 with measurements perturbed by 3% white Gaussian noise. Solid line, dotted line and dashed line represent the true boundary, boundary estimated by EKF, and boundary estimated by UKF, respectively.

and for EKF, it is obtained around the 20th current pattern. As for the 3% white Gaussian noise case, the first stable estimate for UKF is obtained around the 15th current pattern, whereas for EKF, it is around the 35th current pattern. From the reconstructed images of Fig. 11 for 2% white Gaussian noise case, it can be observed that the performance of UKF is better than EKF. The reconstruction results (Fig. 13) for 3% white Gaussian noise show that EKF has nearly failed whereas UKF is still giving a satisfactory performance. Furthermore, UKF is estimating the position well and the only problem is the shape of the target. However, that is expected in noisy scenarios.

In scenario 1, the emphasis was more on the movement of the target and less on the expansion of the target. Therefore, scenario 2 is considered, whose evolution model is given in Fig. 8(b), in which a target initially circular located in south-west, moves north and changes its shape after the application of every current pattern. Here, a total of 48 image frames are considered and in each image frame, one opposite current pattern is used. The parameters used in both UKF and EKF are shown in Table 2. The reconstructed results and RMSE comparison are shown in Figs. 15–20. The reconstructed profiles in Figs. 15, 17 and 19 are shown after every

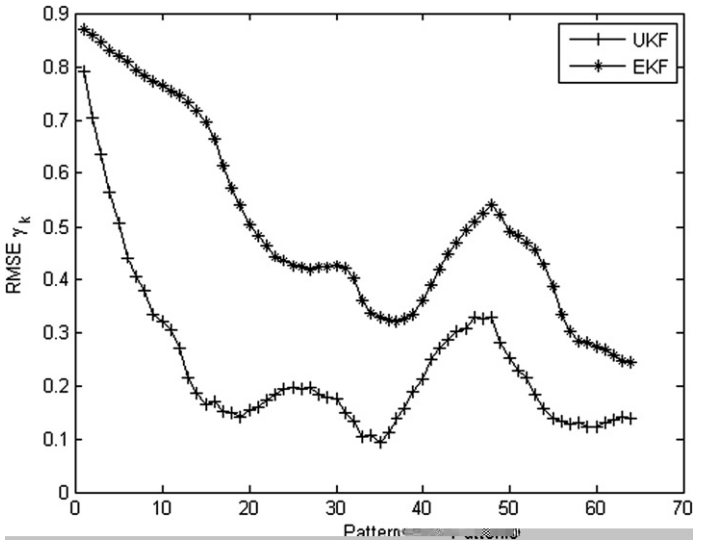

Fig. 14. RMSE comparison for scenario 1 with measurements perturbed by 3% white Gaussian noise.

Table 2
Parameters used in simulations for scenario 2

Parameters	EKF			UKF		
	1% White Gaussian noise	2% White Gaussian noise	3% White Gaussian noise	1% White Gaussian noise	2% White Gaussian noise	3% White Gaussian noise
$\mathbf{Q}$	$0.01\boldsymbol{I}_N$	$0.01\boldsymbol{I}_N$	$0.01\boldsymbol{I}_N$	$0.01\boldsymbol{I}_N$	$0.01\boldsymbol{I}_N$	$0.01\boldsymbol{I}_N$
$\mathbf{R}$	$200\boldsymbol{I}_L$	$1000\boldsymbol{I}_L$	$6000\boldsymbol{I}_L$	$10\boldsymbol{I}_L$	$90\boldsymbol{I}_L$	$300\boldsymbol{I}_L$
$\mathbf{P}_0$	$0.1\boldsymbol{I}_N$	$0.1\boldsymbol{I}_N$	$0.1\boldsymbol{I}_N$	$0.1\boldsymbol{I}_N$	$0.1\boldsymbol{I}_N$	$0.1\boldsymbol{I}_N$
$\bar{\alpha}$	0.001	0.01	0.1	–	–	–
α	–	–	–	0.05	0.08	0.2
β	–	–	–	2	2	2
κ	–	–	–	0	0	0

four current patterns. Here, the changes in the position are not abrupt, therefore, it is anticipated from the first scenario's expansion that the difference between UKF and EKF will be small, however, UKF will still be better in terms of reconstructed image and RMSE. And so, for the 1% white Gaussian noise case, the reconstructed image quality is almost similar for both filters but UKF is slightly better than EKF. In terms of RMSE (Fig. 16), UKF (average RMSE is around 0.05) is performing two times better than EKF (average RMSE is around 0.1). Similarly, for 2% and 3% white Gaussian noise cases, in terms of RMSE (Figs. 18 and 20), the difference between UKF and EKF is small as compared to scenario 1, however, UKF is still performing better than EKF after the application of every current pattern. A similar thing that is already observed in scenario 1 can also be seen in scenario 2 and that is the difference in transition period for higher noise levels.

From the simulation results, it can be established that UKF has performance gains over EKF for processes in which the dynamic changes are abrupt and that it is also possible to model boundaries of air bubbles. Therefore, both UKF and EKF are put to use in experimental studies by considering plastic targets in saline water (with a resistivity of 330 Ω cm). In Fig. 6(c), the possible positions of the plastic targets are shown in the phantom. Since experimental results are a bit difficult to reconstruct and also in the current configuration, the position changes are abrupt, therefore, multiple current injections per image frame are considered during which the target remains stationary. Two different experiments are considered in which UKF and EKF use the parameters shown in Table 3. In both experiments, eight image frames are considered and each image frame

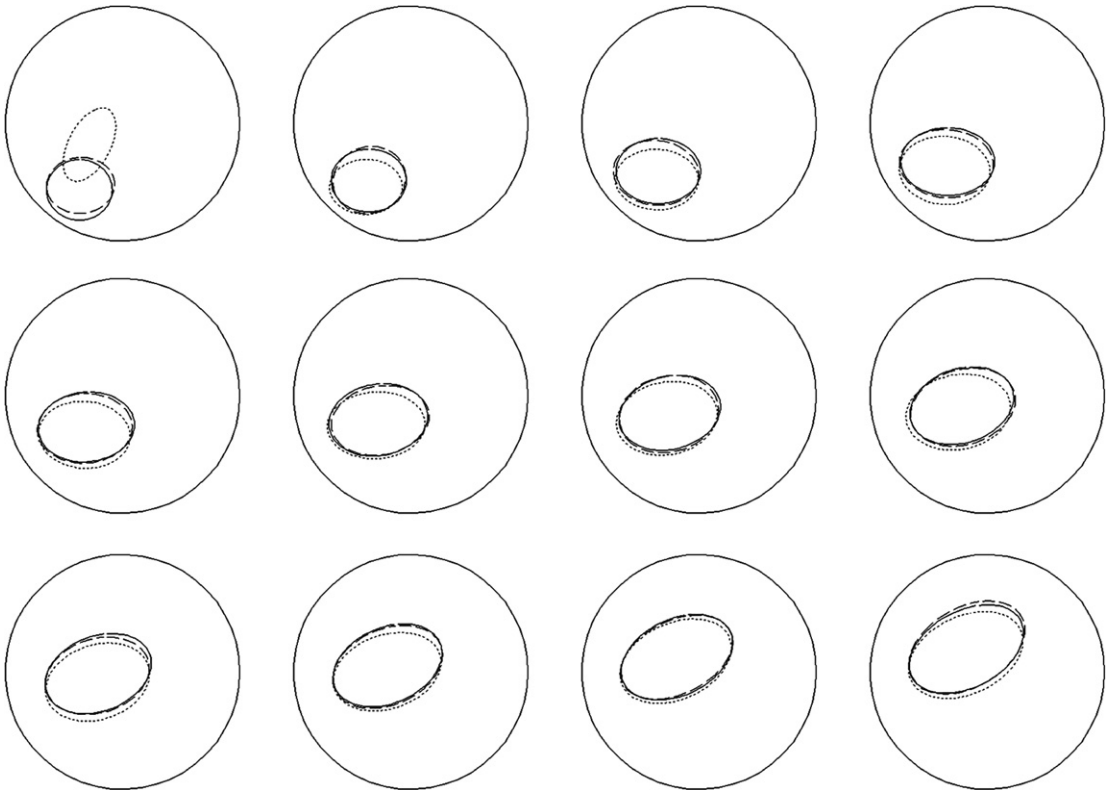

Fig. 15. Reconstructed boundaries for scenario 2 with measurements perturbed by 1% white Gaussian noise. Solid line, dotted line and dashed line represent the true boundary, boundary estimated by EKF, and boundary estimated by UKF, respectively.

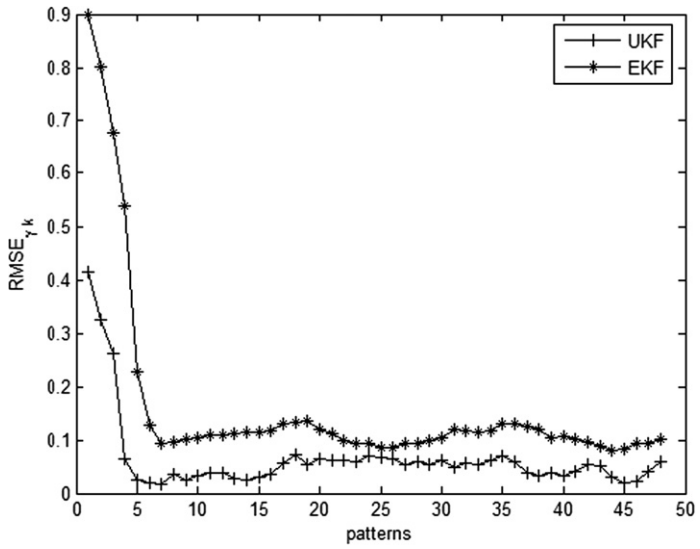

Fig. 16. RMSE comparison for scenario 2 with measurements perturbed by 1% white Gaussian noise.

comprises of six current patterns. The reconstruction results for both experiments are shown in Fig. 21and Fig. 23 after six current patterns and the RMSE comparisons are done in Figs. 22 and 24. In both experiments, it can be seen that UKF is performing far better than EKF in terms of reconstructed boundary. In the RMSE

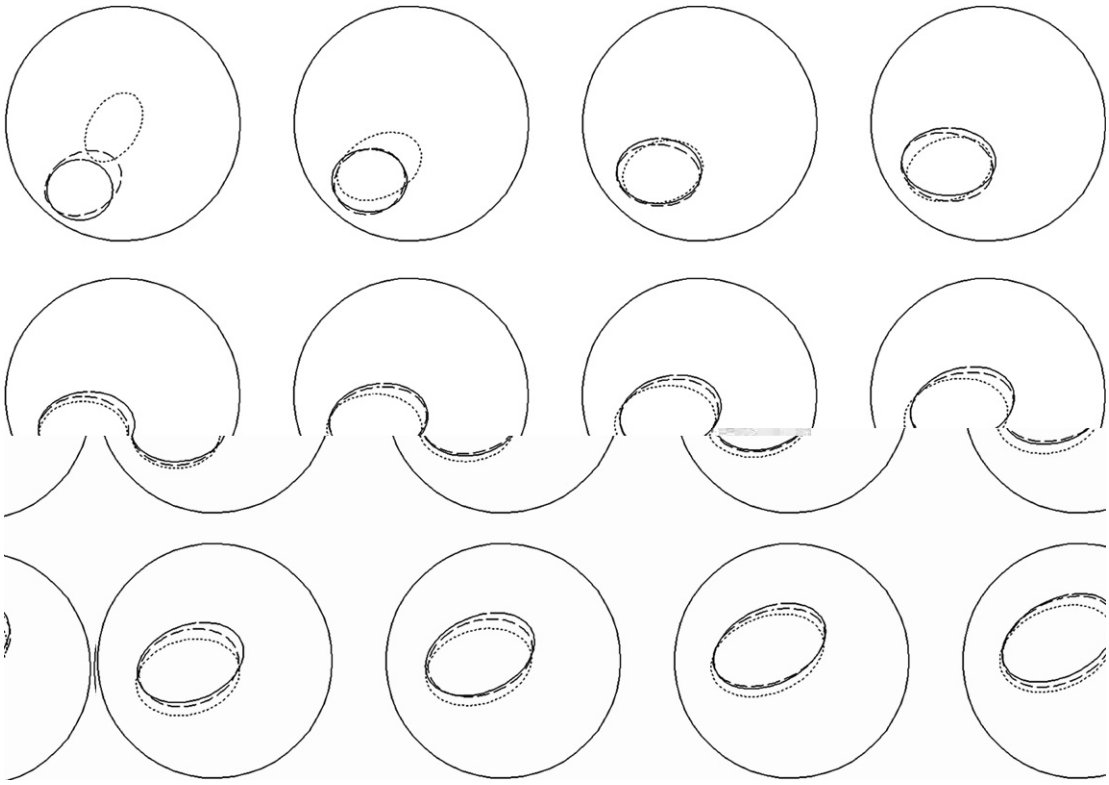

Fig. 17. Reconstructed boundaries for scenario 2 with measurements perturbed by 2% white Gaussian noise. Solid line, dotted line and dashed line represent the true boundary, boundary estimated by EKF, and boundary estimated by UKF, respectively.

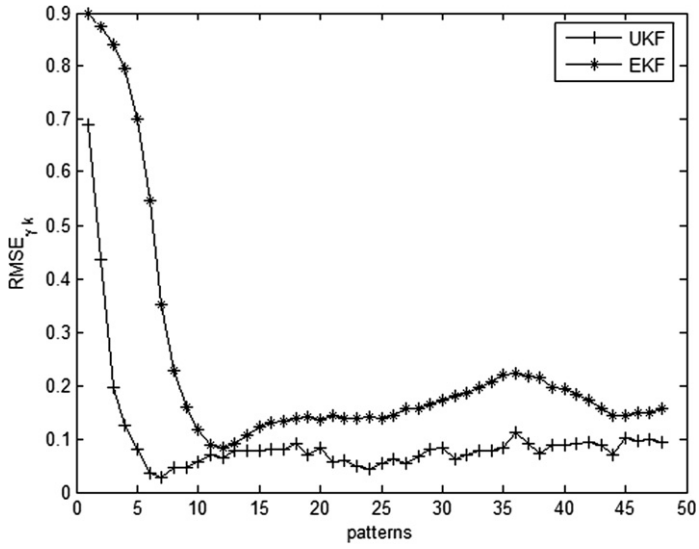

Fig. 18. RMSE comparison for scenario 2 with measurements perturbed by 2% white Gaussian noise.

comparisons (Figs. 22 and 24), it can be seen that mostly the RMSE for UKF is much less than EKF, however, there are certain points where the RMSE curve of both the filters almost come closer. The reason behind this phenomenon is the repetition of the current patterns. Since from the simulations it was observed that

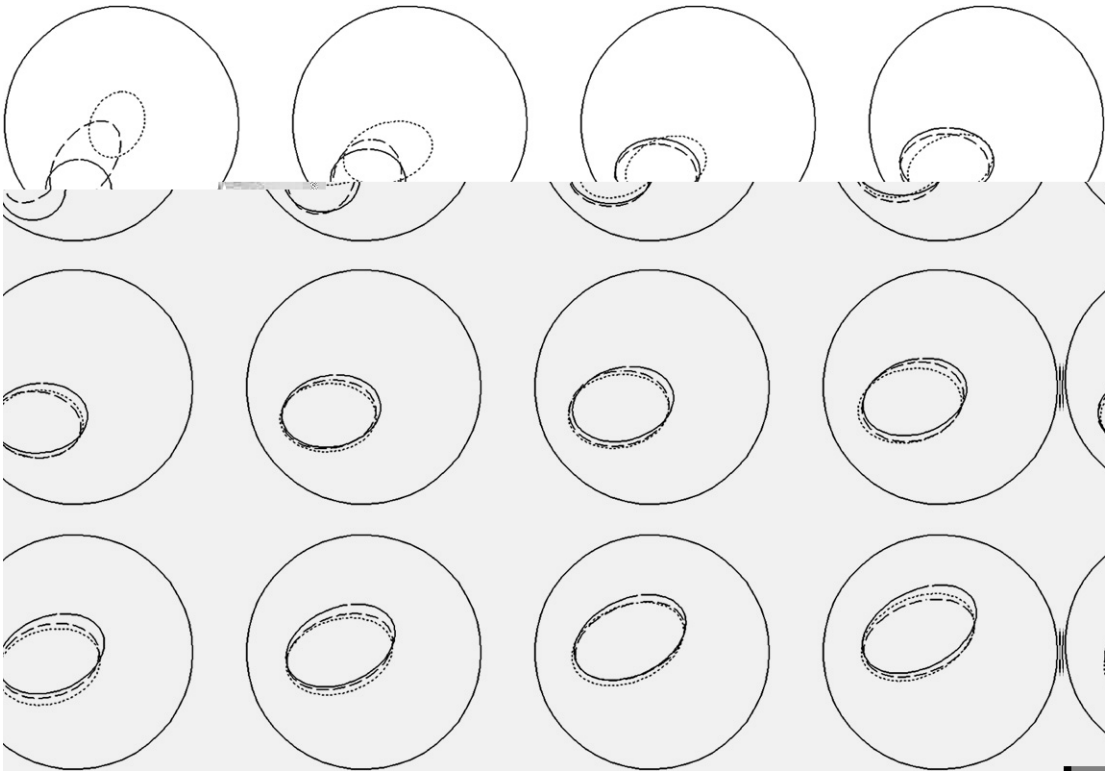

Fig. 19. Reconstructed boundaries for scenario 2 with measurements perturbed by 3% white Gaussian noise. Solid line, dotted line and dashed line represent the true boundary, boundary estimated by EKF, and boundary estimated by UKF, respectively.

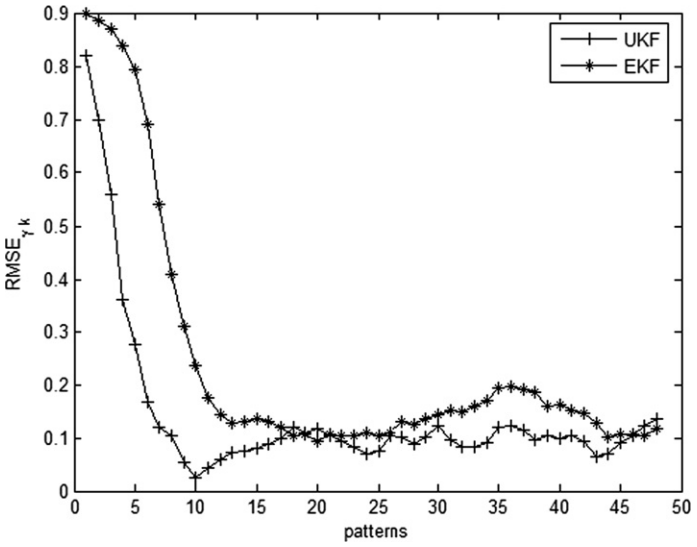

Fig. 20. RMSE comparison for scenario 2 with measurements perturbed by 3% white Gaussian noise.

UKF estimates the position very fast as compared to EKF, therefore, in the first few current patterns in the static case, the decrease in UKF is substantial as compared to EKF. However, after sometimes, when it finally reaches the estimated position, it generally wobbles on the same spot. In the meanwhile, the EKF also con-

Table 3
Parameter used in obtaining experimental results

Parameters	EKF	UKF
$\mathbf{Q}$	$0.01\boldsymbol{I}_N$	$0.01\boldsymbol{I}_N$
$\mathbf{R}$	$200\boldsymbol{I}_L$	$10\boldsymbol{I}_L$
$\mathbf{P}_0$	$0.1\boldsymbol{I}_N$	$0.1\boldsymbol{I}_N$
$\bar{\alpha}$	0.2	–
α	–	0.2
β	–	2
κ	–	0

Fig. 21. Reconstructed boundaries for first experiment. Solid line, dotted line and dashed line represent the true boundary, boundary estimated by EKF, and boundary estimated by UKF, respectively.

verges and hence the difference between UKF and EKF is reduced. In all the simulations and experimental results, it can be noticed that RMSE for UKF is always lower than EKF. This is because UKF basically uses nonlinear unscented transform, and EKF uses the linearized version of the measurement equation. However, there can also be some exception to this rule, i.e., certain scenarios might favor EKF better than UKF which can be best explained from Fig. 25 in which there are three positions of the target. Since UKF estimates fast so it moves very fast to the second position and the slow EKF is still in the middle. However, from the second position to the third position there is more distance for UKF to cover as compared to EKF, thus proving that in certain cases one can also observe EKF's RMSE to be slightly less than that of UKF. The same phenomenon can also be observed in a situation in which a target at position A goes to position B and then comes back to position A. However, through extensive simulations and experimental results, it was found out that such cases are rare and UKF on the average performs better.

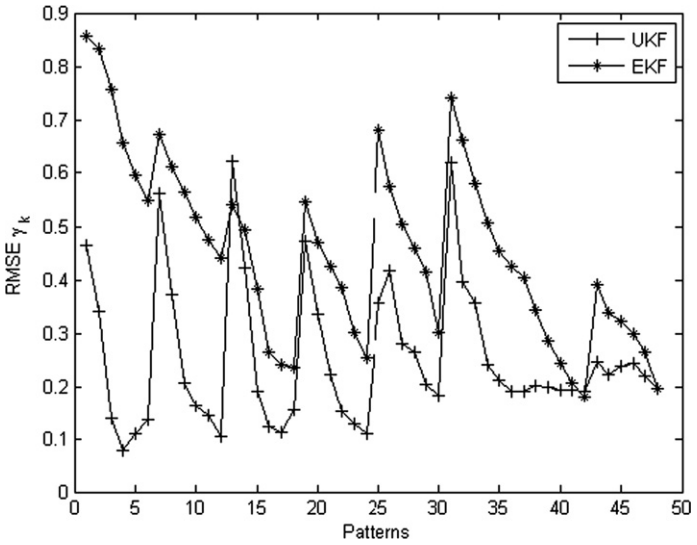

Fig. 22. RMSE comparison for first experiment.

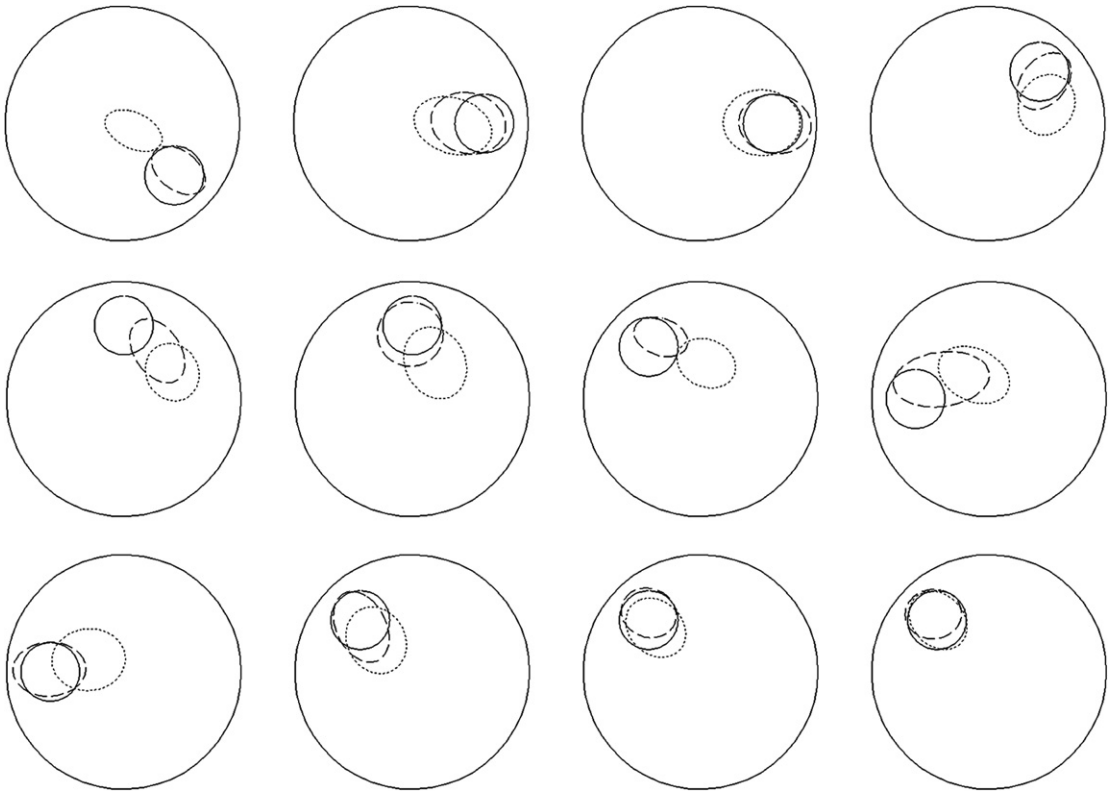

Fig. 23. Reconstructed boundaries for the first experiment. Solid line, dotted line and dashed line represent the true boundary, boundary estimated by EKF, and boundary estimated by UKF, respectively.

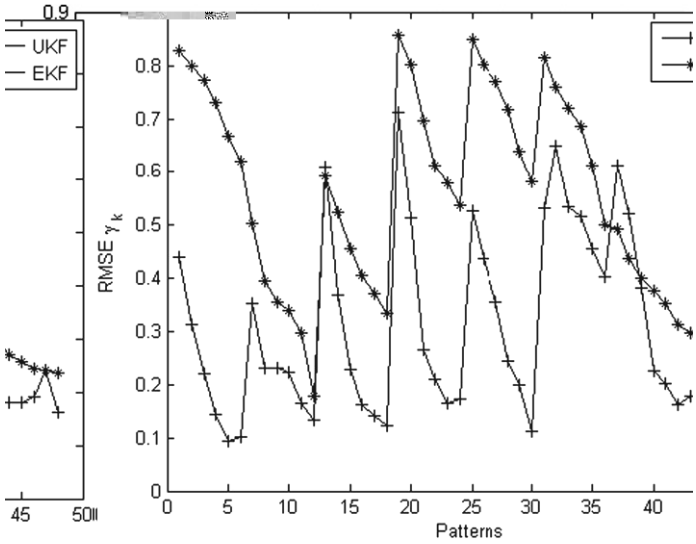

Fig. 24. RMSE comparison for the first experiment.

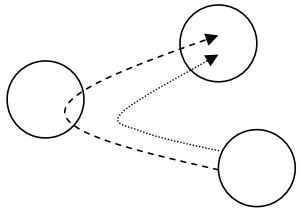

Fig. 25. A scenario favoring EKF. UKF path is represented by dashed line and EKF path is represented by dotted line.

4. Conclusions

In this paper, unscented Kalman filter (UKF) is employed as an inverse solver to estimate the fast transient changes in phase boundary in electrical impedance tomography. The phase boundary is represented by truncated Fourier series. By using UKF as inverse solver, there are several performance gains over conventional extended Kalman filter (EKF). In the case of UKF, the mean and covariance of the state estimate is calculated to second order or better as opposed to the first order in EKF, therefore, UKF always gives better results as compared to EKF. Secondly, no analytical Jacobian is needed to be calculated as the key point in UKF is the nonlinear unscented transform which uses the measurement equation as such. In the past, there were several attempts on more complicated problems in EIT where the internal dynamic equations were difficult to derive, however, in such problems the analytical Jacobian was difficult to derive and so inaccurate numerical methods (like perturbation method) were used in those situations. The choice to choose the three unscented transformation parameters is the only tricky issue. However, mostly in EIT, the assumption is Gaussian, so selection of certain parameters can be done *a priori*, for example, κ and β. In such case, the only parameter needed to be adjusted is the spread parameter α. Therefore, the tuning of UKF does not become difficult anymore and it requires the same number of tunning parameters as required in EKF that uses regularization, i.e., regularization parameter $\bar{\alpha}$ in the case of EKF and α in the case of UKF in addition to **P**, **Q** and **R** which are common in both filters. Regularization can also be considered in UKF but then one has to tune too many parameters and is not desirable. Even without any regularization, UKF is more accurate than EKF as in the case of EKF, the higher-order terms in the Taylor series expansion are ignored while linearizing the measurement Eq. (24). Since the linearization error becomes part of measurement noise so the measurement noise covariance of

EKF is higher than UKF. A higher-order EKF can also be considered to improve accuracy but it then requires the Hessian of the forward solver which is also difficult to obtain.

UKF generates multiple sigma points and thus can be computationally intensive, however, the realizable hardware implementation can take advantage of modern hardware extensions pertaining to vectorization to run some of the UKF code in parallel and thus reducing the computation time. Even in the absence of parallelism, the computational burden can be reduced by limiting the measurement data, i.e, using few current patterns. In this paper, the UKF was used to estimate the changes in phase boundary after the application of a current pattern for nominal changes and for abrupt changes, very few current patterns are used. The simulations and experimental results were done to suggest a practical implication of this research in estimating the boundaries of air bubbles in industrial processes.

Acknowledgement

This work is supported by the research Grant of the Cheju National University in 2007. This work is partially supported by the Korea Science and Engineering Foundation (KOSEF) grant funded by the Korea government (MOST) (No. R01-2007-000-20155-0).

References

[3] J.E. Butler, R.T. Bonnecaze, Inverse method for imaging a free surface using electrical impedance tomography, Chem. Eng. Sci. 55 (2000) 1193–1204.
[4] E.T. Chung, T.F. Chan, X.C. Tai, Electrical impedance tomography using level set representation and total variational regularization, J. Comput. Phys. 205 (2005) 357–372.
[5] Y.V. Fairuzov, Numerical simulation of transient flow of two immiscible liquids in pipeline, AIChE J. 46 (2000) 1332–1339.
[6] D.C. Gisser, D. Isaacson, J.C. Newell, Theory and performance of adaptive current tomography system, Clin. Phys. Hysiol. Meas. 9 (1988) 35–42.
[7] L.F. Gladden, P. Alexander, Application of nuclear magnetic resonance imaging in process engineering, Meas. Sci. Technol. 7 (1996) 423–435.
[8] D.K. Han, A. Prosperetti, A shape decomposition technique in electrical impedance tomography, J. Comput. Phys. 155 (1999) 75–95.
[9] F.A. Holand, R. Bragg, Fluid Flow for Chemical Engineers, Edward Arnold Publisher, London, 1995.
[10] D. Isaacson, Distinguishability of conductivities by electric current computed tomography, IEEE Trans. Medical Imaging M1-5 (1986) 91–95.
[11] O.C. Jones, J.T. Lin, L. Ovacik, H. Shu, Impedance imaging relative to gas–liquid systems, Nucl. Eng. Des. 141 (1993) 159–176.
[12] S.J. Julier, J.K. Uhlmann, A New Extension of the Kalman Filter to nonlinear Systems, in: Proc. of AeroSense: The 11th International Symposium on Aerospace/Defense Sensing, Simulation and Controls, Multi Sensor Fusion, Tracking and Resource Management II, SPIE.
[13] S.J. Julier, J.K. Uhlmann, Unscented filtering and nonlinear estimation, Proc. IEEE 92 (3) (2004) 401–422.
[14] H.J. Jeon, J.H. Kim, B.Y. Choi, K.Y. Kim, M.C. Kim, S. Kim, Electrical impedance imaging of binary mixtures with boundary estimation approach based on multilayer neural network, IEEE Sensors J. 5 (2) (2005) 313–319.
[15] K.Y. Kim, B.S. Kim, M.C. Kim, Y.J. Lee, M. Vauhkonen, Image reconstruction in time-varying electrical impedance tomography based on the extended Kalman filter, Meas. Sci. Technol. 12 (2001) 1–8.
[16] B.S. Kim, M.C. Kim, S. Kim, K.Y. Kim, Nonstationary electrical impedance tomography with the IMM scheme, Meas. Sci. Technol. 15 (2004) 2113–2123.
[17] M.C. Kim, K.Y. Kim, S. Kim, Improvement of impedance imaging for two-phase systems with boundary estimation approach in electrical impedance tomography, Canad. J. Chem. Eng. 83 (2005) 55–63.
[18] K.Y. Kim, B.S. Kim, M.C. Kim, S. Kim, D. Isaacson, J.C. Newell, Dynamic electrical impedance imaging with the interacting multiple model scheme, Physiol. Meas. 26 (2004) S217–S233.
[19] M.C. Kim, S. Kim, K.Y. Kim, Estimation of phase boundaries in two-phase systems by electrical impedance tomography technique, J. Ind. Eng. Chem. 10 (2004) 710–716.
[20] B.S. Kim, U.Z. Ijaz, J.H. Kim, M.C. Kim, S. Kim, K.Y. Kim, Nonstationary phase boundary estimation in electrical impedance tomography based on the interacting multiple model scheme, Meas. Sci. Technol. 18 (2007) 62–70.
[21] J.H. Kim, B.C. Kang, B.Y. Choi, M.C. Kim, S. Kim, K.Y. Kim, Phase boundary estimation in electrical resistance tomography with weighted multilayer neural networks, IEEE Trans. Magnet. 42 (4) (2006) 1191–1194.
[22] M.C. Kim, S. Kim, K.Y. Kim, K.H. Seo, H.J. Jeon, J.H. Kim, B.Y. Choi, Estimation of phase boundary by front points method in electrical impedance tomography, Inverse Prob. Sci. Eng. 14 (2006) 455–466.
[23] J.H. Kim, B.C. Kang, S.H. Lee, B.Y. Choi, M.C. Kim, B.S. Kim, U.Z. Ijaz, K.Y. Kim, S. Kim, Phase boundary estimation in electrical resistance tomography with weighted multi-layered neural networks and front point approach, Meas. Sci. Technol. 17 (2006) 2731–2739.

[24] S. Kim, U.Z. Ijaz, A.K. Khambampati, K.Y. Kim, M.C. Kim, S.I. Chung, Moving interfacial boundary estimation in stratified flow of two immiscible liquids using electrical resistance tomography, Meas. Sci. Technol. 18 (2007) 1257–1269.
[25] V. Kolehmainen, S.R. Arridge, W.R.B. Lionheart, M. Vauhkonen, J.P. Kaipio, Recovery of region boundaries of piecewise constant coefficients of elliptic PDE from boundary data, Inverse Prob. 15 (1999) 1375–1391.
[27] B. Kortschak, B. Brandstätter, A FEM-BEM approach using level-sets in electrical capacitance tomography, Compel 24 (2005) 591–605.
[29] W.R.B. Lionheart, EIT reconstruction algorithms: pitfalls, challenges and recent developments, Physiol. Meas. 23 (2004) 125–142.
[30] J.C. Newell, D.C. Gisser, D. Isaacson, An electric current tomograph, IEEE Trans. Biomed. Eng. 35 (1988) 823–833.
[31] R.H. Perry, D.W. Green, J.O. Maloney, Perry's Chemical Engineers Handbook, McGraw-Hill, New York, 1997.
[32] K.A. Shollenberger, J.R. Torczynski, D.R. Adkin, T.J. O'hern, N.B. Jackson, Gamma-densitometry tomography of gas holdup spatial distribution and industrial-scale bubble column, Chem. Eng. Sci. 52 (1997) 2037–2048.
[34] O.-P. Tossavainen, V. Kolehmainen, M. Vauhkonen, Free-surface and admittivity estimation in electrical impedance tomography, Int. J. Numer. Methods Eng. 66 (2006) 1991–2013.
[35] O.-P. Tossavainen, M. Vauhkonen, V. Kolehmainen, K.Y. Kim, Tracking of moving interfaces in sedimentation processes using electrical impedance tomography, Chem. Eng. J. 61 (2006) 7717–7729.
[36] O.-P. Tossavainen, M. Vauhkonen, L.M. Heikkinen, T. Savolainen, Estimating shape and free surfaces with electrical impedance tomography, Meas. Sci. Technol. 15 (2004) 1402–1411.
[37] O.-P. Tossavainen, M. Vauhkonen, V. Kolehmainen, A three-dimensional shape estimation approach for tracking of phase interfaces in sedimentation process using electrical impedance tomography, Meas. Sci. Technol. 18 (2007) 1413–1424.
[38] R. Van der Merwe, E.R. Wan, The square-root unscented Kalman filter for state and parameter estimation, in: Proceedings of 2001 IEEE International Conference on Acoustics, Speech, and Signal Processing, Salt Lake City, UT, USA, 2001.
[39] M. Vauhkonen, Electrical Impedance Tomography and Prior Information, Ph.D. Thesis, University of Kuopio, Finland, 1997.
[41] M. Vauhkonen, P.A. Karjalainen, J.P. Kaipio, A Kalman filter approach applied to the tracking of fast movements of organ boundaries in electrical impedance tomography, in: Proceedings of 20th Annual International Conference, IEEE, 1998.
[42] M. Vauhkonen, W.R.B. Lionhart, L.M. Heikkinen, P.J. Vauhkonen, J.P. Kaipio, A MATLAB package for the EIDORS project to reconstruct two-dimensional EIT images, Physiol. Meas. 22 (2001) 107–111.
[44] L. Xu, Y. Han, L.A. Xu, J. Yang, Application of ultrasonic tomography to monitoring gas/liquid flow, Chem. Eng. Sci. 52 (1997) 2171–2183.
[45] T.J. Yorkey, J.G. Webster, W.J. Tompkins, Comparing reconstruction algorithms for electrical impedance tomography, IEEE Trans. Biomed. Eng. 34 (1988) 843–852.
[46] S. Osher, J.A. Sethian, Fronts propagating with curvature dependent speed: algorithms based on Hamilton–Jacobi formulations, J. Comput. Phys. 79 (1988) 12–49.
[47] L. Rondi, F. Santosa, Enhanced electrical impedance tomography via the Mumford–Shah functional, ESAIM: control, Optim. Calc. Variat. 6 (2001) 517–538.
[48] T.F. Chan, X.-C. Tai, Level set and total variation regularization for elliptic inverse problems with discontinuous coefficients, J. Comput. Phys. 193 (2003) 40–66.
[49] T.F. Chan, X.-C. Tai, Identification of discontinuous coefficients from elliptic problems using total variation regularization, SIAM J. Sci. Comput. 25 (2003) 881–904.
[50] L.A. Vese, T.F. Chan, A new multiphase level set framework for image segmentation via the Mumford and Shah model, Int. J. Comput. Vision 50 (3) (2002) 271–293.
[51] M. Soleimani, Electrical impedance tomography imaging using *a priori* ultrasound data, Biomed. Eng. Online (2006) 5–8.
[52] M. Soleimani, W.R.B. Lionheart, O. Dorn, Level set reconstruction of conductivity and permittivity from boundary electrical measurement using experimental data, Inverse Prob. Sci. Eng. 14 (2) (2006) 193–210.
[53] M. Soleimani, O. Dorn, W.R.B. Lionheart, A narrow-band level set method applied to EIT in brain for cryosurgery monitoring, IEEE Trans. Biomed. Eng. 53 (11) (2006) 2257–2264.
[54] K. Van den doel, U.M. Ascher, On level set regularization for highly ill-posed distributed parameter estimation problems, J. Comput. Phys. 216 (2006) 707–723.